Int. J. Corros. Scale Inhib., 2025, **14**, no. 1, 353–380

Exploring geranium essential oil as a sustainable corrosion inhibitor for XC48 carbon steel in 1 M HCl

W. Zriouel,[1] M. Oubahou[2] and B. Hammouti[3*]

[1] *Laboratory of Engineering and Materials (LIMAT), Faculty of Sciences Ben M'sick, Hassan II University of Casablanca, 7955, Casablanca, Morocco*
[2] *Laboratory of Physical Chemistry of Materials, Faculty of Sciences Ben M'sick, Hassan II University of Casablanca, 7955, Casablanca, Morocco*
[3] *Euromed Research Center, Euro-Mediterranean University of Fes, BP 51, Fes 30070, Morocco*
**E-mail: hammoutib@gmail.com*

Abstract

This study explores the effectiveness of geranium essential oil (GEO) as an environmentally sustainable corrosion inhibitor for XC48 carbon steel in a 1 M HCl solution. The chemical composition of GEO, characterized by GC/FID, identified geraniol (19.53%) and β-citronellol (17.25%) as the main components. Electrochemical analyses, including potentiodynamic polarization (PDP) and electrochemical impedance spectroscopy (EIS), indicated that GEO functions as a mixed-type inhibitor, achieving a maximum inhibition efficiency of 89.82% at a concentration of 2.0 g/L. Gravimetric analysis further showed a significant decrease in corrosion rate with increasing GEO concentration, though inhibition efficiency declined at elevated temperatures (298–328 K), likely due to the desorption of inhibitor molecules from the steel surface. Activation energy (E_a) values increased with GEO concentration, suggesting the formation of a physical adsorption layer that hinders corrosion. Positive activation enthalpy (ΔH^*) values confirmed the endothermic nature of the steel dissolution process, while increased entropy (ΔS^*) with GEO concentration pointed to enhanced system disorder due to water displacement on the surface. Computational modeling provided additional insights, with quantum chemical calculations pointing to (*E*)-citral and citronellyl tiglate as particularly reactive constituents based on favorable electronic properties. Monte Carlo simulations corroborated these findings by highlighting strong interactions between specific GEO molecules, such as β-citronellol and α-costol, and the steel surface. The results confirm that GEO offers a promising eco-friendly alternative to conventional corrosion inhibitors.

Received: December 20, 2024 Published: March 22, 2025 doi: 10.17675/2305-6894-2025-14-1-22

Keywords: *carbon steel, corrosion inhibition, Monte Carlo simulation, activation energy, geranium essential oil.*

1. Introduction

Steel is widely used in various industries due to its exceptional properties and high resistance in different environments. However, in certain industrial processes involving acidic conditions, carbon steel is susceptible to corrosion. To mitigate this problem, effective protection strategies must be implemented. There are several methods of preventing corrosion, but many of them are very costly. Among these, the use of corrosion inhibitors is a cost-effective and efficient solution for minimizing corrosion damage.

In recent years, plant extracts have received particular attention as environmentally-friendly corrosion inhibitors for metals in a variety of environments [1–4]. These natural extracts contain bioactive compounds, which can adsorb onto metal surfaces, forming a protective layer that reduces corrosion [5, 6]. Extensive research has demonstrated the effectiveness of plant-based inhibitors in various corrosive environments, making them a promising alternative to synthetic inhibitors, which are often associated with environmental concerns and high production costs [7–9]. According to the literature, the corrosion-inhibiting properties of plant derivatives are mainly attributed to their rich composition of bioactive molecules. Compounds such as saponins, phenolic components, polysaccharides, proteins and various organic molecules containing heterocyclic structures or electronegative atoms such as nitrogen (N), oxygen (O) and sulfur (S) play a crucial role in metal protection. These components, which possess π-electrons and functional groups capable of interacting with metal surfaces, facilitate the formation of an adsorbed protective layer. This adsorption mechanism significantly reduces metal degradation in corrosive environments, reinforcing the potential of plant-based inhibitors as a durable and effective solution for corrosion control.

The aim of this research is to investigate the efficacy of GEO as a green corrosion inhibitor for XC48 carbon steel in acidic environments. The study combines electrochemical methods with computational modeling to evaluate the inhibitory properties of the essential oil on the corrosion process. By analyzing the interaction between the bioactive compounds in the essential oil and the steel surface, both experimentally and theoretically, we aim to understand the mechanisms involved and assess its potential as an eco-friendly alternative to conventional chemical inhibitors.

2. Materials and Methods

2.1. Steel composition and aggressive solution

In this study, the working electrode was made from XC48 carbon steel with the chemical composition presented in Table 1. The cylindrical electrode was covered with Teflon, leaving a surface area of 0.5 cm^2 exposed to the test solution for electrochemical measurements. Rectangular carbon steel coupons ($25\times10\times10\ \text{mm}^3$) were used for gravimetric tests. All experiments were carried out in triplicate in aerated, stagnant solutions at the desired temperature. Before each measurement, the carbon steel electrode was polished with Sic paper up to 1500 grit, washed with distilled water and dried. The 1 M HCl solution was prepared by diluting reagent-grade concentrated HCl (37%) with double-distilled water.

Table 1. Chemical constituents of XC48 carbon steel.

Elements	**C**	**Si**	**Mn**	**Ni**	**Cr**	**P**	**S**	**Mo**	**Fe**
Percentage	0.46	0.23	0.64	0.19	0.09	0.014	0.010	0.02	98.346

2.2. Characterization of the GEO

The GEO was analyzed using gas chromatography on a Clarus 580 PerkinElmer GC system, coupled with a flame ionization detector (FID). A RESTEK column (60 m, 0.25 mm ID, 0.25 μm) was used for the analysis.

2.3. Electrochemical measurements

The electrochemical behavior of XC48 carbon steel in the hydrochloric acid was studied using potentiodynamic polarization (PDP) and electrochemical impedance spectroscopy (EIS). A conventional three-electrode configuration was employed, with a saturated calomel electrode (SCE) serving as the reference electrode, a platinum plate as the counter electrode, and the XC48 carbon steel as the working electrode. The experiments were performed using a PGZ100 potentiostat/galvanostat controlled by Voltamaster 4. Before each test, the XC48 steel electrode was immersed in the test solution for 30 minutes to allow stabilization of the open circuit potential (OCP) at a temperature of 298 K. PDP measurements were taken at a scan rate of 1 mV/s, within a potential range of –800 to –200 mV. EIS tests were conducted with a frequency range of 100 kHz to 10 mHz and a signal amplitude of 10 mV. The EIS data were adjusted and analyzed using EC-LAB software.

2.4. Weight loss measurements

The XC48 steel samples with dimensions of $25\times10\times10$ mm^3 were weighed and immersed in hydrochloric acid for 24 hours, both with and without varying concentrations of GEO. The experiments were conducted across a temperature range of 298–328 K. After 24 hours of exposure, the samples were removed from the test solutions, and corrosion products were carefully removed using a sharp brush. The samples were then washed with distilled water and acetone, dried, and reweighed using a precision balance to assess the corrosion rate.

2.5. Computational considerations

2.5.1. Molecular quantum descriptor

All calculations were conducted using the 2020 version of Materials Studio Software [10]. The computational study began with the optimization of the molecules using Density

Functional Theory (DFT). To better understand the molecular mechanisms underlying corrosion inhibition, various quantum parameters of the constituents in GEO were calculated. These parameters included the energies of the Highest Occupied Molecular Orbital (HOMO) and Lowest Unoccupied Molecular Orbital (LUMO), the electronic energy gap ($\Delta\varepsilon$), as well as absolute electronegativity (χ), hardness (η), and softness (σ). The calculations were performed based on Koopmans' theorem via the following relationships as previously reported in literature [11–13].

Table 2. Quantum parameters.

The quantum parameters	**Calculation equation**
The highest occupied molecular orbital	$I = -\varepsilon_{\text{HOMO}}$
The lowest unoccupied molecular orbital	$A = -\varepsilon_{\text{LUMO}}$
The electronic gap	$\Delta\varepsilon = \varepsilon_{\text{LUMO}} - \varepsilon_{\text{HOMO}}$
The absolute electronegativity	$\chi = -\mu_{\text{i}} = -\left(\frac{\varepsilon_{\text{LUMO}} + \varepsilon_{\text{HOMO}}}{2}\right)$
The absolute hardness	$\eta = \frac{\varepsilon_{\text{LUMO}} - \varepsilon_{\text{HOMO}}}{2}$
The softness	$\sigma = \frac{1}{\eta} = \frac{2}{\varepsilon_{\text{LUMO}} - \varepsilon_{\text{HOMO}}}$
The fraction of electrons transferred ΔN in the interaction of mild steel and the GEO	$\Delta N = \frac{\chi_{\text{Fe}} - \chi_{\text{inh}}}{2(\eta_{\text{Fe}} + \eta_{\text{inh}})}$ where $\chi_{\text{Fe}} = 7\ \text{eV}\cdot\text{mol}^{-1}$ and $\eta_{\text{Fe}} = 0\ \text{eV}\cdot\text{mol}^{-1}$ [14]
The electrophilicity index expresses the ability of an electrophile to acquire an electronic charge	$\omega = \frac{\chi^2}{2\eta}$

2.5.2. Monte Carlo simulations

Monte Carlo simulation can efficiently predict the adsorption behavior under different environmental conditions, thereby helping to understand the inhibitor's effectiveness in preventing corrosion [15]. This technique is particularly useful for identifying how factors like molecular structure and surface properties influence the interaction between the inhibitor and the metal, leading to more accurate predictions of corrosion inhibition performance. In the present work, we perform a geometric optimization, for each molecule contained in GEO, using the Forcite module in Materials Studio software [10]. Subsequently, the adsorption energy of the interaction between all molecules and the iron surface, specifically the Fe (110) surface, is calculated using the adsorption Locator module. The Fe (110) surface was selected for its stability [16] during the simulation in the gas phase. For the aqueous phase, a water molecule is introduced into the simulation through the adsorption Locator module.

3. Results and Discussions

3.1. Chemical composition of the GEO

The results of the characterization of GEO by GC/FID are summarized in Table 3.

Table 3. Chemical composition of the GEO.

Molecule	2D structure of compound	Percentage %	Molecule	2D structure of compound	Percentage %
α-pinene $C_{10}H_{16}$	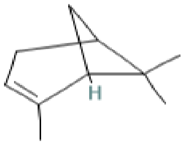	1.62	Germacrene D $C_{15}H_{24}$	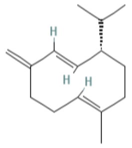	0.24
Linalol $C_{10}H_{18}O$	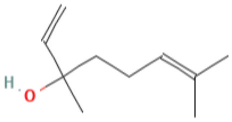	9.01	Viridiflore $C_{15}H_{27}NO_4$	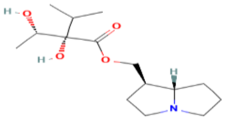	0.62
Cis-rose oxide $C_{10}H_{18}O$	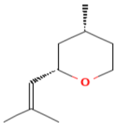	0.3	α-muurolene $C_{15}H_{24}$	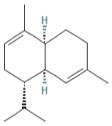	0.5
Trans-rose oxide $C_{10}H_{18}O$	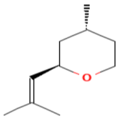	3.13	Geranyl butyrate $C_{14}H_{24}O_2$	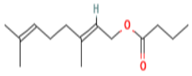	0.12
Iso-Menthone $C_{10}H_{18}O$	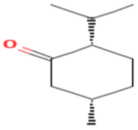	8.63	Trans-caryophyllene $C_{15}H_{24}$	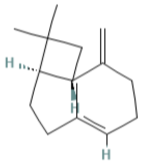	0.38
β-citronellol $C_{10}H_{20}O$		17.25	Geranyl propionate $C_{13}H_{22}O_2$	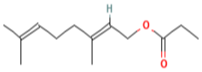	0.39

Molecule	2D structure of compound	Percentage %	Molecule	2D structure of compound	Percentage %
α-Terpineol $C_{10}H_{18}O$	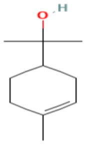	1.61	γ-cadinene $C_{15}H_{24}$	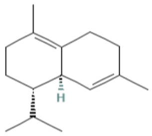	2.98
Citronellol $C_{10}H_{20}O$	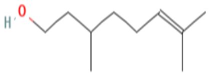	8.27	10-epi-g-eudesmol $C_{15}H_{26}O$	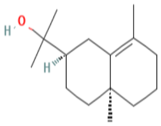	6.56
Geraniol $C_{10}H_{18}O$	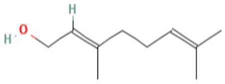	19.53	Citronellyl acetate $C_{12}H_{22}O_2$	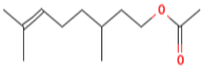	0.22
(*E*)-citral $C_{10}H_{16}O$	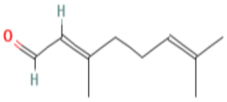	0.53	α-Costol $C_{15}H_{24}O$	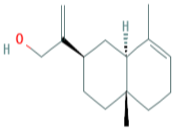	0.14
Neryl formate $C_{11}H_{18}O_2$	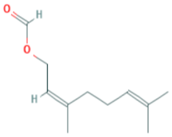	0.24	2-phenethyl tiglate $C_{13}H_{16}O_2$	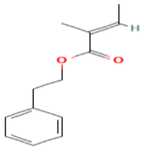	0.36
Nerol $C_{10}H_{18}O$	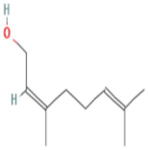	2.09	α-Selinene $C_{15}H_{24}$	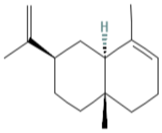	0.75
Citronellyl formate $C_{11}H_{20}O_2$	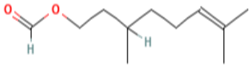	7.67	Citronellyl tiglate $C_{15}H_{26}O_2$	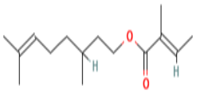	0.26
β-bourbonene $C_{15}H_{24}$	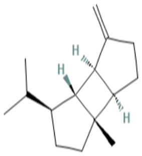	1.74	Geranyl tiglate $C_{15}H_{24}O_2$	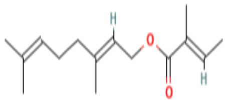	0.87
Geranyl formate $C_{11}H_{18}O_2$	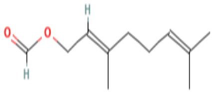	3.21	Citronellyl ester $C_{11}H_{20}O_2$	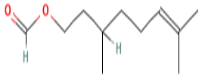	0.39

The GEO characterization reveals a complex mixture of components with varying concentrations. Geraniol (19.53%) and β-citronellol (17.25%) are the dominant constituents, which are well-known for their beneficial properties and significant roles in the oil's overall effectiveness. These major components are likely to be the primary contributors to the oil's potential as a corrosion inhibitor, given their known interactions with metal surfaces [17]. Additionally, compounds like citronellol (8.27%), iso-menthone (8.63%), 10-*epi*-*g*-eudesmol (6.56%) and citronellyl formate (7.67%) also can play a significant role in the oil's efficacy. Although many compounds are present in smaller quantities, such as α-pinene (1.62%) and α-terpineol (1.61%), their cumulative effect should not be overlooked as they may contribute to the overall inhibitory action. In order to explore the effect of this complex mixture of molecules on the corrosion of XC48 steel, we are carrying out an electrochemical study which will be confirmed by a computational study.

3.2. Electrochemical measurements

a. Potentiodynamic polarization (PDP)

The potentiodynamic polarization technique is a valuable tool for calculating electrochemical parameters [17–18]. It enables oxidation or reduction reactions at the metal surface by generating sufficient current, as demonstrated by the polarization curves of the test electrode over a wide potential range. Figure 1 illustrates the semi-logarithmic polarization curves for mild steel in 1 M HCl solution, both with and without GEO at varying concentrations. These curves provide critical insights into the electrochemical behavior of mild steel and the corrosion inhibition properties of GEO.

Generally, the dissolution of iron in HCl solution is primarily influenced by the adsorbed intermediate species $(\mathrm{FeCl})_{\mathrm{ads}}$, as outlined in the following reaction mechanism:

$$\mathrm{Fe} + \mathrm{Cl}^- \rightleftarrows \left(\mathrm{FeCl}^-\right)_{\mathrm{ads}}$$

$$\left(\mathrm{FeCl}^-\right)_{\mathrm{ads}} \rightleftarrows \left(\mathrm{FeCl}\right)_{\mathrm{ads}} + e^- \left(\mathrm{FeCl}\right)_{\mathrm{ads}} \rightarrow \mathrm{FeCl}^+ + e^-$$

$$\mathrm{FeCl}^+ + e^- \rightarrow \mathrm{Fe}^{2+} + \mathrm{Cl}^-$$

The cathodic reaction involved in this process is the generation of hydrogen gas, which occurs through the reduction of hydrogen ions:

$$\mathrm{Fe} + \mathrm{H}^+ \rightleftarrows \left(\mathrm{FeH}^+\right)_{\mathrm{ads}}$$

$$\left(\mathrm{FeH}^+\right)_{\mathrm{ads}} + e^- \rightleftarrows \left(\mathrm{FeH}\right)_{\mathrm{ads}}$$

$$\left(\mathrm{FeH}\right)_{\mathrm{ads}} + \mathrm{H}^+ + e^- \rightarrow \mathrm{Fe} + \mathrm{H}_2$$

It is clear from Figure 1 that the carbon steel in the blank solution exhibits a corrosion potential (E_{corr}) of −487.1 mV versus the SCE reference electrode. Both anodic and cathodic current densities increase due to activation mechanisms driven by overpotentials. Besides, the Tafel slopes reveal that anodic dissolution is increasingly suppressed with higher concentrations of GEO, while the cathodic hydrogen evolution reaction is also impacted, particularly at 1.0 g/L, where a notable change in the cathodic slope (β_c) occurs [19, 20].

As the inhibitor concentration rises, its suppressive effect on both anodic and cathodic processes becomes more pronounced, indicating that inhibitor molecules adsorb onto active sites on the mild steel surface, preventing further reactions [21].

It is widely recognized that inhibitor molecules adsorb onto a metal surface by displacing one or more previously adsorbed water molecules. This process can be described as follows:

$$\text{Inh}_{\text{sol}} + x\text{H}_2\text{O}_{\text{ads}} \leftrightarrow \text{Inh}_{\text{ads}} + x\text{H}_2\text{O}_{\text{ads}}$$

In the above equation, Inh_{sol} refers to the inhibitor present in the solution, whereas Inh_{ads} denotes the inhibitor that has adsorbed onto the surface.

Consequently, the inhibitor molecules interact with the Fe^{2+} ions generated on the steel surface, forming a complex between the metal and the inhibitor.

$$\text{Fe} \rightarrow \text{Fe}^{2+} + 2e^-$$

$$\text{Fe}^{2+} + \text{Inh}_{\text{ads}} \rightarrow \left(\text{Fe} - \text{Inh}\right)^{2+}_{\text{ads}}$$

Table 4 presents the electrochemical parameters derived from the PDP curves, including corrosion potential (E_{corr}), corrosion current density (i_{corr}), and inhibition efficiency (IE%). The table highlights the enhanced corrosion resistance of the system, demonstrating the effectiveness of GEO in reducing corrosion. The inhibition efficiency is calculated using the following formula [22]:

$$E_{\text{PDP}} = \frac{i_{\text{corr}} - i_{\text{inh}}}{i_{\text{corr}}} \cdot 100 \tag{4}$$

where i_{corr} and i_{inh} represent the corrosion current density values in the absence and presence of the inhibitor, respectively, both determined by extrapolating the cathodic Tafel lines to the corrosion potential.

Inspection of the results presented in Table 4 shows that the corrosion potential of XC48 steel shifts slightly towards more negative values compared to the blank sample, with a displacement of less than 85 mV, confirming GEO as a mixed-type inhibitor [2–12]. Moreover, the corrosion current density decreases from 1.09 mA/cm^2 (without inhibitor) to 0.11 mA/cm^2 at 2 g/L GEO, indicating a lower corrosion rate [4]. The inhibition efficiency E_{PDP} increases significantly with concentration, reaching approximately 90% at 2 g/L [23]. This behavior is attributed to the molecular structure of the inhibitor and donor-acceptor interactions between the empty d-orbitals of Fe atoms and the essential oil components [24]. However, these findings should be further validated using complementary techniques like Electrochemical Impedance Spectroscopy (EIS) and weight loss measurements to confirm the inhibitor's performance.

Table 4. Electrochemical parameters of XC48 steel at different concentrations of the GEO in 1.0 M HCl and corresponding inhibition efficiencies.

Concentration of GEO, g/l	E_{corr}, mV	i_{corr}, mA/cm^2	β_a, mV/dec	β_c, mV/dec	E_{PDP}, %
0.0	−487.1±1.7	1.090±0.008	163.3±1.2	−110.0±3.6	–
0.5	−503.2±1.9	0.395±0.012	109.3±1.8	−122.4±2.7	63.76±0.13
1.0	−487.5±1.7	0.346±0.005	121.4±2.2	−240.2±1.4	68.26±0.04
1.5	−555.3±1.2	0.221±0.011	142.7±0.8	−111.7±2.8	79.72±0.13
2.0	−535.1±0.5	0.111±0.004	103.5±0.9	−119.9±0.9	89.82±0.03

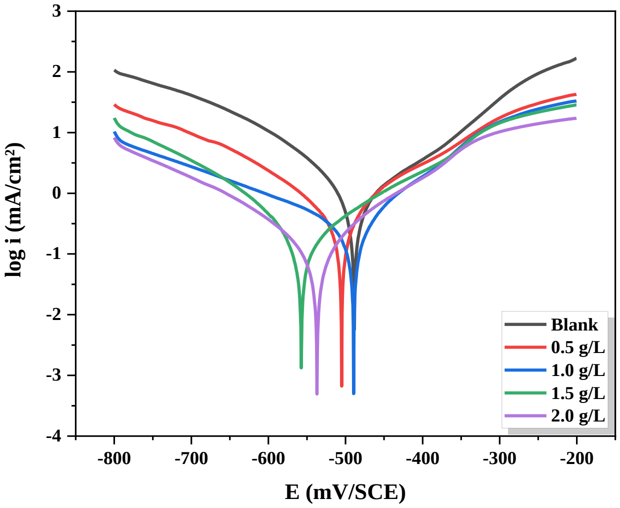

Figure 1. Potentiodynamic curves for XC48 steel in 1.0 M HCl in the presence of the GEO at different concentrations.

b. Electrochemical impedance spectroscopy

EIS is a widely used, non-destructive technique that provides critical insights into the physical and electronic properties of electrochemical systems. In corrosion inhibition studies, it enables detailed analysis of the metal/solution interface. The Nyquist plots in this study were used to evaluate the impedance and conductivity of XC48 carbon steel in 1 M HCl, offering valuable information about the corrosion rate and the metal's resistance to corrosion [25]. Figure 2 shows the Nyquist plots, which display a single capacitive loop, indicating that the charge transfer process predominantly controls the corrosion mechanism

[26]. The consistent shape of the spectra across all concentrations suggests that the essential oil does not alter the corrosion mechanism of mild steel [27]. As the essential oil concentration increases, the surface coverage improves, leading to a larger semicircle diameter. Additionally, Figure 3 presents Bode plots for XC48 steel in 1.0 M HCl at 298 K, with and without GEO at different concentrations. The log(z) values increase progressively, indicating enhanced corrosion resistance. This improvement is attributed to the formation of a protective layer on the metal surface, where the adsorbed essential oil acts as a barrier against the corrosive medium [28]. The single-phase peak in the Bode phase diagrams suggests the presence of only one time constant, associated with the double-layer behavior and charge transfer process during carbon steel corrosion [2].

The experimental data were analyzed using the EC-Lab software and the electrical equivalent circuits (EEC) depicted in Figure 5. The EEC comprises key components, including R_s (solution resistance), R_{ct} (charge transfer resistance), Q_{dl} (constant phase element associated with the double-layer capacitance). During the fitting process, the ideal capacitor (C_{dl}) was replaced with CPE to account for the non-ideal capacitive behavior of the electrode, which arises from surface inhomogeneity.

The impedance of the CPE is described by the following equation, which depends on Q and n parameters [29].

$$Z_{CPE} = Q^{-1}(j\omega)^{n}$$

Herein, Q represents the CPE constant, ω is the angular frequency, j is an imaginary number, n is the CPE exponent, which serves as an indicator of surface roughness of the metal.

The use of the equivalent circuit allows us to determine the concerned electrochemical parameters as well as IE, which are listed in Table 5. The chi-square (χ^2) values obtained after fitting are below 10^{-3}, indicating that the difference between the fitted values and the experimental data is minimal, which reinforces the reliability of the selected equivalent circuit.

The inhibition efficiency of GEO (E_{EIS}) was calculated based on the charge transfer resistance using the following equation [30].

$$E_{\text{EIS}} = \frac{R_{\text{ct,inh}} - R_{\text{ct,0}}}{R_{\text{ct,inh}}} \cdot 100 \tag{5}$$

where $R_{\text{ct,inh}}$ and $R_{\text{ct,0}}$ represent the charge transfer resistance in the presence and the absence of the GEO.

As the concentration of the GEO increases, there is a significant rise in charge transfer resistance (R_{ct}), from 17.11 Ω·cm^2 for the blank sample to 148.19 Ω·cm^2 at a concentration of 2.0 g/L. Additionally, the double-layer capacitance (C_{dl}) decreases notably, from 89.63 to 11.47 μF·cm^2, which can be explained by a reduction in the local dielectric constant and/or an increase in the thickness of the double layer. This suggests that the essential oil likely adsorbs onto the surface of the steel submerged in 1.0 M HCl [31]. Also, the slight deviation of the n value from unity is attributed to the constant phase element (CPE) deviating from ideal capacitive behavior, likely due to surface irregularities caused by the formation of a porous layer on the metal surface [32]. Moreover, the inhibition efficiency (E_{EIS}) increases with higher GEO concentrations, reaching a maximum value of 88.45% at 2.0 g/L. The EIS results confirm the findings obtained using PDP, demonstrating that GEO exhibits effective inhibitory properties.

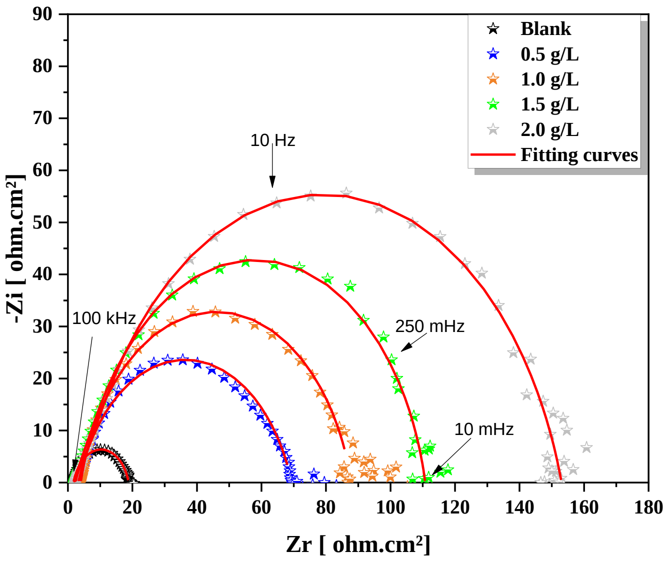

Figure 2. Nyquist plots of XC48 carbon steel in 1 M HCl for different concentrations of GEO at 294 K.

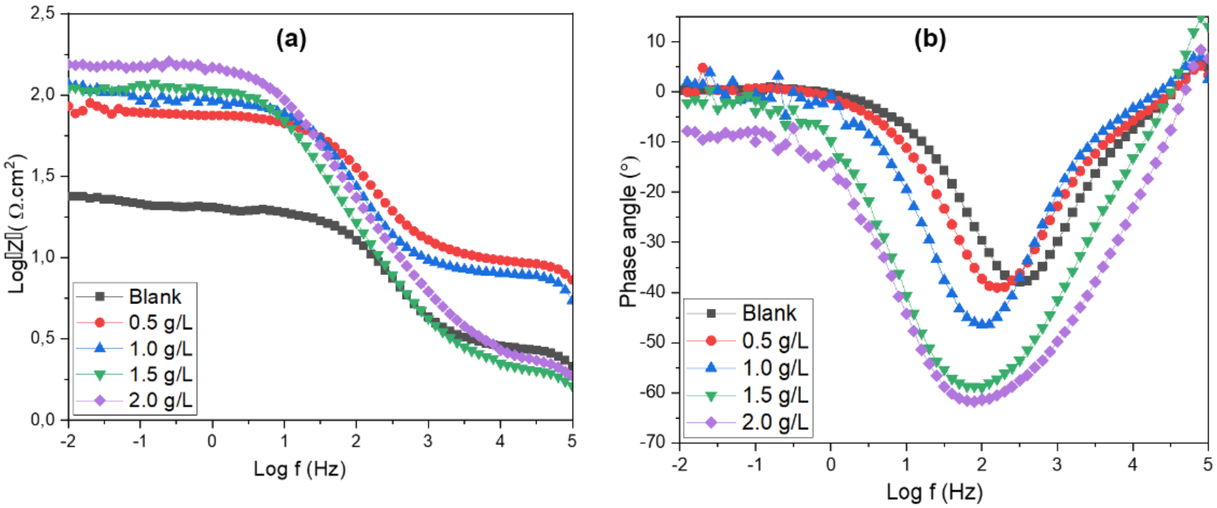

Figure 3. Bode diagrams for XC48 steel in 1 M HCl without and with the inhibitor at various concentrations.

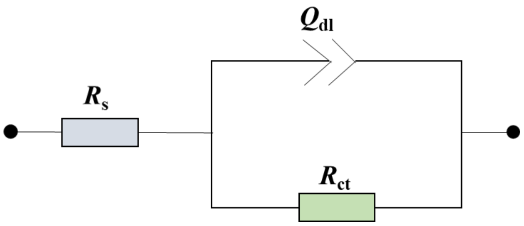

Figure 4. Scheme of the equivalent circuit used to fit EIS data of GEO in 1 M HCl.

The inhibition efficiency of GEO (IE_{EIS}%) was calculated based on the charge transfer resistance using the following equation [24].

$$E_{EIS} = \frac{R_{ct,inh} - R_{ct,0}}{R_{ct,inh}} \cdot 100 \tag{6}$$

where $R_{ct,inh}$ and $R_{ct,0}$ represent the charge transfer resistance in the presence and the absence of the GEO.

Table 5. Electrochemical impedance parameters and *IE*eis% for XC48 carbon steel corrosion in 1 M HCl without and with various concentrations of GEO at 294 K.

Concentration of GEO, g/l	R_s, **Ω·cm²**	R_{ct}, **Ω·cm²**	C_{dl}, **μF/cm²**	n	$\chi^2 \cdot 10^{-3}$	E_{EIS}, **%**
0.0	1.73	17.11±0.50	89.63±0.66	0.81	0.22	–
0.5	3.24	66.15±1.14	26.04±1.52	0.79	1.45	74.13±0.30
1.0	3.95	83.93±1.22	20.39±0.89	0.84	0.89	79.61±0.29
1.5	2.08	104.30±0.98	14.17±0.15	0.87	1.02	83.59±0.27
2.0	2.22	148.19±1.36	11.47±0.21	0.81	0.73	88.45±0.23

3.3. Weight loss

Weight loss measurement is a widely employed technique for assessing corrosion and evaluating the effectiveness of corrosion inhibitors in various materials [33]. This method offers key insights into the corrosion rate and the performance of inhibitors by determining the reduction in mass of a sample due to corrosion. In the present study, weight loss analysis was conducted after immersing the carbon steel samples in a 1 M HCl solution for 24 hours. The inhibition efficiency of GEO (E_W) was calculated as follows [34]:

$$E_W = \frac{W_0 - W_{inh}}{W_{inh}} \cdot 100 \tag{7}$$

$$C_R = \frac{W_b - W_a}{At} \cdot 100 \tag{8}$$

where W_0 and W_{inh} correspond to the corrosion weight losses of the mild steel in the absence and presence of the inhibitor. The variables W_b and W_a represent the weight of the specimen before and after immersion in the test solution, respectively. A is the total surface area of the carbon steel specimen (in cm^2), and t present the exposure time (in hours). The obtained results are calculated and presented in Table 6.

The data presented in Table 6 show that GEO exhibited exceptional inhibition efficiency in protecting XC48 steel from corrosion in this environment. The untreated steel samples, represented in the blank column, had a corrosion rate (C_R) of 1.542 mg/(cm^2·h). However, the inhibited samples by GEO at concentrations ranging from 0.5 to 2 g/l displayed a marked reduction in corrosion rates, with the lowest C_R observed at 2 g/l, reaching 0.242 mg/(cm^2·h).

As the inhibitor concentration increased, the inhibition efficiency (IE_W) improved significantly, rising from 69.19% at 0.5 g/l to 84.31% at 2 g/l. This indicates that GEO is effective in mitigating the corrosion of XC48 steel in a 1 M HCl medium. Moreover, surface coverage (θ) increased with higher inhibitor concentrations, suggesting that the inhibitor molecules adsorb onto the metal surface, forming a protective layer that slows down the corrosion process [35]. These results highlight the potential of GEO as an efficient corrosion inhibitor for carbon steel in acidic environments.

Table 6. Corrosion parameters values for XC48 carbon steel in 1 M HCl in the absence and the presence of different concentrations of GEO, after 24 h immersion period at 294 K.

Concentration, g/l	**C_R, mg/(cm^2·h)**	**E_W, %**	**θ**
Blank	1.542±0.045	–	–
0.5	0.475±0.016	69.19±0.13	0.6920
1.0	0.374±0.026	75.74±0.95	0.7575
1.5	0.291±0.011	81.13±0.16	0.8113
2.0	0.242±0.021	84.31±0.88	0.8431

3.4. Temperature effect and activation parameters

Corrosion inhibitors and substrates often display varying behavior in aggressive media, especially at elevated temperatures. Figure 5. represents the effect of temperature on corrosion inhibition in the absence and the presence of different concentration of the GEO.

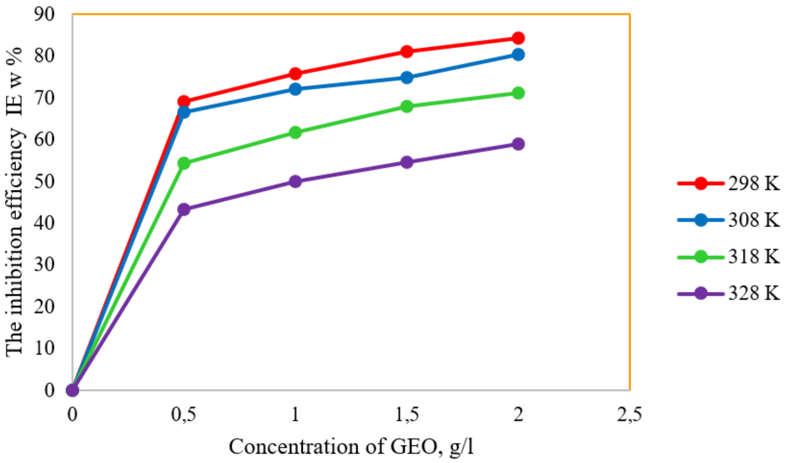

Figure 5. Effect of temperature on corrosion inhibition.

As the temperature increases, GEO molecules become more soluble and tend to desorb from the metallic surface. This leads to a reduction in steel's corrosion resistance with rising temperatures [36]. In this study, gravimetric analysis was carried out at three additional temperatures (308 K, 318 K and 328 K) using varying concentrations of GEO (0.5–2.0 g/l) to evaluate the effect of temperature on the inhibition efficiency (*IE*%) of GEO. The results, presented in Table 7, highlight how different concentrations of the essential oil influence corrosion rates across these temperature conditions.

Table 7. Corrosion parameters values for XC48 carbon steel in 1 M HCl in the absence and the presence of different concentrations of GEO, after 24 h immersion period, at 298 K, 308 K, 318 K and 328 K.

Conc., g/l	**298 K**		**308 K**		**318 K**		**328 K**	
	C_R, mg/(cm^2·h)	**E_W, %**	**C_R, mg/(cm^2·h)**	**E_W, %**	**C_R, mg/(cm^2·h)**	**E_W, %**	**C_R, mg/(cm^2·h)**	**E_W, %**
Blank	1.542	–	2.347	–	4.139	–	5.436	–
0.5	0.475	69.19	0.785	66.55	1.891	54.31	3.085	43.25
1.0	0.374	75.74	0.655	72.09	1.586	61.68	2.713	50.09
1.5	0.291	81.13	0.589	74.90	1.322	68.06	2.463	54.69
2.0	0.242	84.31	0.459	80.44	1.194	71.15	2.226	59.05

Across all temperatures, the inhibition efficiency *(E%)* increased as the concentration of GEO increased, indicating that the inhibitor progressively adsorbed onto the steel surface. However, as the temperature rose from 298 K to 328 K, the *E*% decreased significantly (from 84.31% to 59.05%), while the corrosion rate increased (from 0.242 to 2.226 mg/(cm^2·h)) at the highest concentration of GEO. This suggests that at higher temperatures, the inhibitor is more prone to desorption from the steel surface [37]. The adsorption of GEO is likely facilitated by the presence of numerous electrons within the molecular structure of its components, particularly π electrons. These characteristics enhance its ability to bind effectively to the metal surface, improving its performance as a corrosion inhibitor [25].

To further understand this temperature dependence, kinetic parameters such as activation energy (E_a), activation enthalpy (ΔH^*), and activation entropy (ΔS^*) were evaluated. These parameters provide deeper insight into the corrosion inhibition mechanism. By applying the Arrhenius and transition state equations (Equations 6 and 7), these kinetic parameters were determined based on the weight loss data obtained at different temperatures. This analysis offers a clearer understanding of how the GEO interacts with the steel surface across varying temperatures [26].

$$\log C_R = \frac{-E_a}{2.303RT} + \log A \tag{9}$$

$$C_R = \frac{RT}{Nh}\exp\left(\frac{\Delta S_a}{R}\right)\exp\left(-\frac{\Delta H_a}{RT}\right) \tag{10}$$

where C_R stand for the corrosion rate the studied metal, A is the Arrhenius pre-exponential factor, R represents the gas constant, N is Avogadro's number, T is the absolute temperature, and h is Planck's constant.

Arrhenius plots for the dissolution of XC48 carbon steel in 1 M HCl, both with and without the presence of GEO as an inhibitor, are presented in Figure 6.

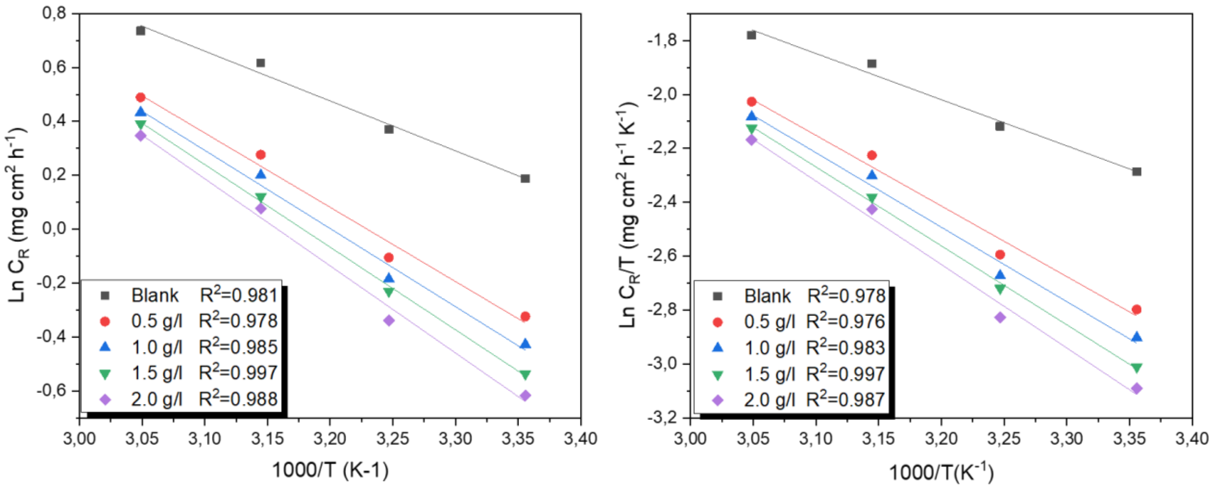

Figure 6. Arrhenius plots for the dissolution of XC48 carbon steel in 1 M HCl, both with and without the presence of GEO.

The corresponding activation parameters, including activation energy (E_a), activation enthalpy (ΔH^*), and activation entropy (ΔS^*), are summarized in Table 8.

Table 8. Activation parameters values for XC48 carbon steel in 1 M HCl in the absence and the presence of different concentration of GEO.

Concentration, g/l	E_a, kJ/mol	ΔH^*	ΔS^*
Blank	7.05	14.24	–187.91
0.5	22.90	21.77	–167.08
1.0	24.09	22.96	–163.92
1.5	25.47	24.34	–160.09
2.0	26.85	25.73	–156.23

As shown in Table 8, the activation energy (E_a) for carbon steel corrosion in blank 1 M HCl is 7.05 kJ/mol. However, when GEO is introduced at varying concentrations, the E_a values increase significantly. This increase indicates that the corrosion process becomes more difficult in the presence of the GEO [38]. At the highest concentration of 2 g/l, the activation energy reaches 26.85 kJ/mol. This shift in activation energies suggests that the inhibitor forms an electrostatic barrier between the carbon steel surface and the corrosive medium, effectively reducing corrosion [39]. Additionally, the fact that the maximum E_a remains below the threshold for chemical adsorption (80 kJ/mol) implies that the adsorption of GEO onto the steel surface is primarily physical [4]. This physical adsorption likely forms a protective layer, preventing direct contact between the metal and the corrosive environment, thereby improving the inhibition efficiency. The positive values of ΔH^* (activation enthalpy) observed both with and without the essential oil confirm that the dissolution process of carbon steel is endothermic [40]. Similarly, the trend in activation entropy (ΔS^*) reflects changes in E_a, increasing with higher concentrations of GEO. This increase in ΔS^* is attributed to the desorption of water molecules from the metal surface as essential oil molecules adsorb, leading to an increase in the overall entropy of the system [41].

3.5. Computational study of the inhibition behavior of GEO

a. Quantum parameters

The optimized geometric structures, along with the HOMO and LUMO orbitals of all the molecules of the GEO, are presented in Table 9. The quantum parameters of the all of molecules included in GEO, obtained using DFT calculations in the Dmol^3 module of Materials Studio Software, are summarized in Table 10.

Table 9. The optimized geometric structures, along with the HOMO and LUMO orbitals of all the molecules included in GEO.

Molecule	HOMO	LUMO	Molecule	HOMO	LUMO	Molecule	HOMO	LUMO	Molecule	HOMO	LUMO
α-Pinene	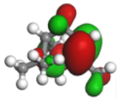	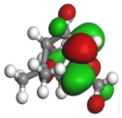	Geraniol	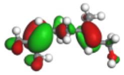	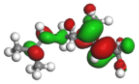	Germacrene D	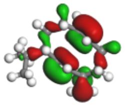	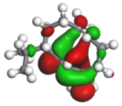	10-*epi*-*g*-Eudesmol	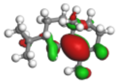	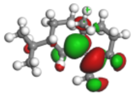
Linalool	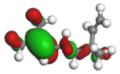	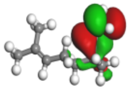	(*E*)-Citral	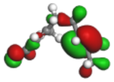	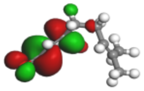	Viridiflore	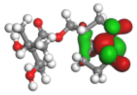	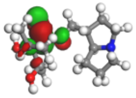	Citronellyl acetate	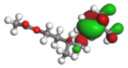	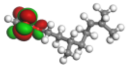
cis-Rose oxide	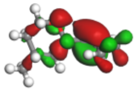	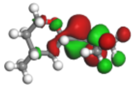	Neryl formate	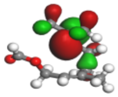	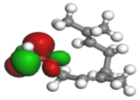	α-Muurolene	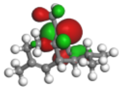	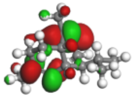	α-Costol	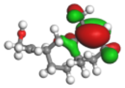	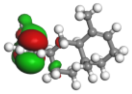
trans-Rose oxide	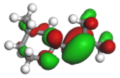	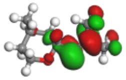	Nerol	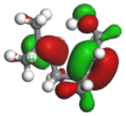	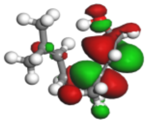	Geranyl butyrate	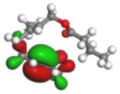	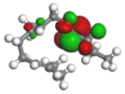	2-Phenethyl tiglate	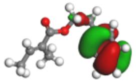	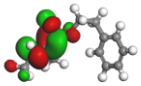
iso-Menthone	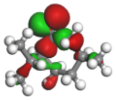	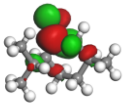	Citronellyl formate	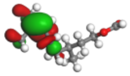	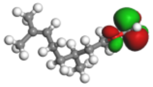	*trans*-Caryophyllene	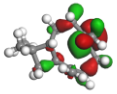	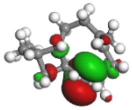	α-Selinene	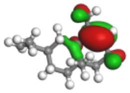	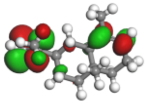
β-Citronellol	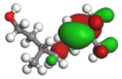	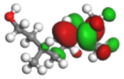	β-Bourbonene	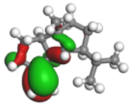	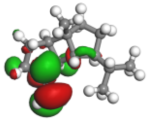	Geranyl propionate	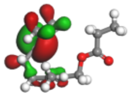	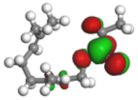	Citronellyl tiglate	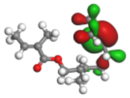	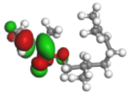
α-Terpineol	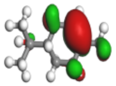	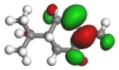	Geranyl formate	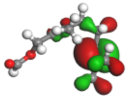	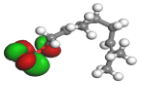	γ-Cadinene	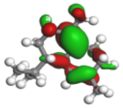	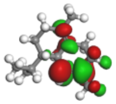	Geranyl tiglate	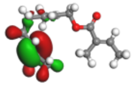	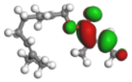
Citronellol	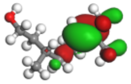	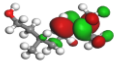	Citronellyl ester	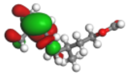	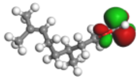						

Table 10. The Quantum parameters of all of the all of molecules of the GEO obtained by Dmol^3/DFT calculation.

Parameter	**E_{HOMO}, eV**	**E_{LUMO}, eV**	**ΔE**	**χ, eV**	**η, eV**	**σ, eV^{-1}**	**ω, eV**
α-pinene	–5.823	1.13	6.953	2.347	3.477	0.288	0.792
Linalool	–6.1	0.36	6.46	2.870	3.230	0.310	1.275
cis-rose oxide	–6.118	0.996	7.114	2.561	3.557	0.281	0.922
Trans-rose oxide	–5.992	1.091	7.083	2.451	3.542	0.282	0.848
Iso-Menthone	–6.272	–0.471	5.801	3.372	2.901	0.345	1.959
β-citronellol	–6.165	0.987	7.152	2.589	3.576	0.280	0.937
α-Terpineol	–5.82	1.449	7.269	2.186	3.635	0.275	0.657
Citronellol	–6.164	0.985	7.149	2.590	3.575	0.280	0.938
Geraniol	–5.973	0.728	6.701	2.623	3.351	0.298	1.026
(*E*)-citral	–6.402	–1.454	4.948	3.928	2.474	0.404	3.118
Neryl formate	–6.119	–0.148	5.971	3.134	2.986	0.335	1.644
Nerol	–6.285	0.656	6.941	2.815	3.471	0.288	1.141
Citronellyl formate	–6.177	–0.28	5.897	3.229	2.949	0.339	1.768
β-bourbonene	–6.163	0.838	7.001	2.663	3.501	0.286	1.013
Geranyl formate	–6.151	–0.269	5.882	3.210	2.941	0.340	1.752
Citronellyl ester	–6.177	–0.28	5.897	3.229	2.949	0.339	1.768
Germacrene D	–5.294	0.241	5.535	2.527	2.768	0.361	1.153
Viridiflore	–5.197	–0.504	4.693	2.851	2.347	0.426	1.731
α-muurolene	–5.93	1.115	7.045	2.408	3.523	0.284	0.823
Geranyl butyrate	–5.874	0.078	5.952	2.898	2.976	0.336	1.411
trans-caryophyllene	–5.808	0.86	6.668	2.474	3.334	0.300	0.918
Geranyl propionate	–5.992	0.1	6.092	2.946	3.046	0.328	1.425
γ-cadinene	–5.673	1.194	6.867	2.240	3.434	0.291	0.730
10-epi-g-eudesmol	–5.674	1.219	6.893	2.228	3.447	0.290	0.720
Citronellyl acetate	–6.15	–0.017	6.133	3.084	3.067	0.326	1.550
α-Costol	–5.958	0.381	6.339	2.789	3.170	0.316	1.227
2-phenethyl tiglate	–6.421	–0.915	5.506	3.668	2.753	0.363	2.444
α-Selinene	–5.962	1.114	7.076	2.424	3.538	0.283	0.830
Citronellyl tiglate	–6.036	–0.869	5.167	3.453	2.584	0.387	2.307
Geranyl tiglate	–6.027	–0.789	5.238	3.408	2.619	0.382	2.217

The quantum parameters reveal important insights into the corrosion inhibition potential of the molecules in GEO. Molecules with higher E_{HOMO} values, such as Germacrene D and Viridiflore, are better electron donors, facilitating stronger adsorption on the steel surface [41]. A smaller energy gap (Δε), as seen in (*E*)-citral and Citronellyl tiglate, indicates higher reactivity and enhanced inhibition efficiency [42]. Higher electronegativity (χ), as observed in (*E*)-citral and Citronellyl tiglate, suggests better electron-accepting ability, promoting their interaction with the metal [43]. Softer molecules (higher σ), like (*E*)-citral and Viridiflore, are more reactive and interact better with the steel surface, while higher electrophilicity (ω) in molecules like (*E*)-citral and 2-phenethyl tiglate further enhances their inhibition efficiency [44, 15]. Overall, we can conclude that (*E*)-citral and Citronellyl tiglate emerge as highly effective inhibitors due to their favorable quantum parameters, while molecules like α-Terpineol and β-citronellol may be less efficient.

b. Monte Carlo simulation

The energies obtained from the Monte Carlo simulation in both aqueous and gas phases are shown in Table 11. In this analysis, the adsorption energy refers to the energy released or absorbed when the adsorbate, in its relaxed and unrelaxed forms, adheres to the substrate. The deformation energy refers to the energy released when the adsorbed component of the adsorbate undergoes relaxation on the substrate surface [45].

Table 11. The results of the Monte Carlo simulation of the molecules constituting GEO in gas and aqueous phases

Molecule	**Phases**	**Total energy, kcal/mol**	**Adsorption energy, kJ/mol**	**Rigid adsorption energy kJ/mol**	**Deformation energy, kJ/mol**	**$dE_{\mathrm{ad}}/dE_{\mathrm{Ni}}$**
Iron (110) + α-pinene	Gas phase	−79.477	−79.224	−80.116	0.892	−79.224
	Aqueous phase	−4638.905	−4638.905	−4937.800	298.894	−69.115
Iron (110) + Linalool	Gas phase	−130.946	−91.577	−97.710	6.133	−91.577
	Aqueous phase	−4764.988	−4764.988	−5038.292	273.303	−127.632
Iron (110) + α-Terpineol	Gas phase	−132.761	−87.158	−91.030	3.871	−87.158
	Aqueous phase	−4227.559	−4227.559	−4501.095	273.535	−108.562
Iron (110) + Germacrene D	Gas phase	−111.955	−104.494	−106.483	1.989	−104.494
	Aqueous phase	−3998.261	−3998.261	−4338.014	339.752	−90.463
Iron (110) + *cis*-rose oxide	Gas phase	−125.697	−92.720	−98.607	5.886	−92.720
	Aqueous phase	−337.227	−337.27	−404.494	67.267	0.239

Molecule	**Phases**	**Total energy, kcal/mol**	**Adsorption energy, kJ/mol**	**Rigid adsorption energy kJ/mol**	**Deformation energy, kJ/mol**	**dE_{ad}/ dE_{Ni}**
Iron (110) + *trans*-rose oxide	Gas phase	–118.812	–87.164	–91.264	4.099	–87.164
	Aqueous phase	–3489.582	–3489.582	–3778.204	288.621	–24.034
Iron (110) + *iso*-Menthone	Gas phase	–96.870	–83.954	–84.875	0.920	–83.954
	Aqueous phase	–3322.344	–3322.344	–3571.947	249.602	–46.023
Iron (110) + Beta-Citronellol	Gas phase	–114.542	–91.136	–95.024	3.887	–91.136
	Aqueous phase	–3323.379	–3323.379	–3717.755	394.376	–62.498
Iron (110) + Citronellol	Gas phase	–113.182	–89.775	–91.045	1.269	–89.775
	Aqueous phase	–3695.501	–3695.501	–3945.843	250.341	–60.126
Iron (110) + Geraniol	Gas phase	–111.445	–92.446	–96.378	3.932	–92.446
	Aqueous phase	–3746.951	–3746.953	–4018.790	271.837	–70.828
Iron (110) + *E*-Citral	Gas phase	–149.885	–86.457	–90.692	4.234	–86.4579
	Aqueous phase	–4120.914	–4120.916	–4397.395	276.479	–89.409
Iron (110) + Neryl Formate	Gas phase	–118.223	–99.769	–106.011	6.241	–99.769
	Aqueous phase	–4063.505	–4063.505	–4417.916	354.410	–119.308
Iron (110) + Nerol	Gas phase	–116.454	–93.396	–95.438	2.042	–93.396
	Aqueous phase	–3609.054	–3609.054	–3840.253	231.199	–88.902
Iron (110) + Citronellyl formate	Gas phase	–127.835	–108.231	–110.928	2.697	–108.231
	Aqueous phase	–3213.830	–3213.830	–3562.169	348.338	–71.033
Iron (110) + β-bourbonene	Gas phase	–116.463	–103.019	–106.055	3.036	–103.019
	Aqueous phase	–2883.143	–2883.143	–3177.316	294.173	–64.426
Iron (110) + Geranyl formate	Gas phase	–132.627	–114.947	–117.721	2.774	–114.947
	Aqueous phase	–3162.985	–3162.985	–3485.409	322.423	–59.473
Iron (110) + Viridiflorine	Gas phase	–148.110	-168.049	–175.027	6.978	–168.049
	Aqueous phase	–2750.257	–2750.257	–3012.203	261.945	–54.049
Iron (110) + α-muurolene	Gas phase	–139.046	–109.676	–111.370	1.693	–109.676
	Aqueous phase	–3082.864	–3082.864	–3366.598	283.733	–63.137

Molecule	**Phases**	**Total energy, kcal/mol**	**Adsorption energy, kJ/mol**	**Rigid adsorption energy kJ/mol**	**Deformation energy, kJ/mol**	**dE_{ad}/dE_{Ni}**
Iron (110) + Geranyl butyrate	Gas phase	−157.655	−133.507	−139.983	6.475	−133.507
	Aqueous phase	−3268.122	−3268.122	−3541.974	273.852	−63.898
Iron (110) + *trans*-caryophyllene	Gas phase	−121.589	−109.409	−111.754	2.344	−109.409
	Aqueous phase	−2938.206	−2938.206	−3219.879	281.673	−68.121
Iron (110) + Geranyl propionate	Gas phase	−137.581	−120.806	−123.342	2.536	−120.806
	Aqueous phase	−3168.737	−3168.737	−3417.985	249.247	−86.707
Iron (110) + Δ-Cardinene	Gas phase	−132.243	−107.080	−109.841	2.760	−107.080
	Aqueous phase	−2772.333	−2772.333	−3024.590	252.257	−53.085
Iron (110) + 10-*epi*-*g*-eudesmol	Gas phase	−164.837	−116.270	−118.558	2.288	−116.270
	Aqueous phase	−3278.423	−3278.423	−3516.875	238.452	−71.105
Iron (110) + Citronellyl acetate	Gas phase	−152.225	−116.789	-121.619	4.829	−116.789
	Aqueous phase	−2867.846	−2867.846	−3156.170	288.324	−63.624
Iron (110) + α-Costol	Gas phase	−139.222	−121.099	−125.177	4.078	−121.099
	Aqueous phase	−3269.685	−3269.685	−3695.077	425.391	−83.799
Iron (110) + 2-phenethyl tiglate	Gas phase	−142.935	−119.471	−121.960	2.489	−119.471
	Aqueous phase	−3562.149	−3562.149	−3832.524	270.374	−69.430
Iron (110) + alpha-Selinene	Gas phase	−141.413	−108.237	−111.442	3.204	−108.237
	Aqueous phase	−3086.285	−3086.285	−3337.419	251.133	−85.057
Iron (110) + Citronellyl tiglate	Gas phase	−183.622	−139.092	−145.530	6.437	−139.092
	Aqueous phase	−3070.615	-3070.615	−3298.513	227.897	−69.292
Iron (110) + Geranyl tiglate	Gas phase	−176.757	−136.456	−141.513	5.056	−136.456
	Aqueous phase	−3131.545	−3131.545	−3447.440	315.895	−73.549
Iron (110) + Citronellyl ester	Gas phase	−144.762	−109.326	−112.951	3.624	−109.326
	Aqueous phase	−3059.700	−3059.700	−3319.748	260.048	−55.372

According to the results presented in Table 11, the Monte Carlo simulation results reveal that GEO molecules generally demonstrate higher adsorption energies and stronger affinities to the Fe (110) surface in aqueous environments than in the gas phase, indicating enhanced inhibition potential in the presence of water. Notably, molecules such as α-costol, citronellyl tiglate, E-citral, and geranyl tiglate exhibit high adsorption and total energies, forming stable, resilient complexes with iron that contribute to their effectiveness as corrosion inhibitors. High deformation energies in molecules like α-costol (425.391 kJ/mol) suggest structural flexibility, allowing them to conform closely to the metal surface and establish an adaptable protective barrier.

Additionally, molecules with high dEad/dENi values, such as geraniol and β-citronellol, exhibit significant interaction strengths, supporting their potential for stable adsorption layer formation. Conversely, molecules with lower adsorption and deformation energies, such as iso-menthone (0.920 kJ/mol in the gas phase), may provide more rigid but less adaptable protection.

Differences in isomer structure, such as between cis- and trans-rose oxide, underscore how molecular geometry can affect adsorption characteristics. For instance, cis-rose oxide's lower rigid adsorption energy (–404.494 kJ/mol in the aqueous phase) could make it especially suited for stable barrier formation under certain conditions. Overall, molecules like α-costol, citronellyl tiglate, and geranyl tiglate emerge as particularly effective constituents for corrosion inhibition on iron surfaces, leveraging their high adsorption energy, adaptability, and robust surface interactions in aqueous environments.

In the Table 12, we present the optimal configurations of simulations for the various molecules of GEO in gas and aqueous phases obtained by Monte Carlo.

4. Conclusion

This study demonstrates that GEO is an effective green corrosion inhibitor for XC48 carbon steel in 1 M HCl. The major components, geraniol (19.53%) and β-citronellol (17.25%), contribute significantly to its inhibitory performance through adsorption on the steel surface, forming a protective layer. Electrochemical analyses confirm GEO as a mixed-type inhibitor, with inhibition efficiency reaching 89.82% at 2.0 g/L. EIS results support this by showing increased charge transfer resistance and decreased double-layer capacitance. Weight loss measurements further validate the reduction in corrosion rate with increasing GEO concentration. Regarding temperature effects, the studies reveal that inhibition efficiency decreases at higher temperatures due to the desorption of GEO molecules, indicating a physically dominant adsorption mechanism. Quantum chemical calculations and Monte Carlo simulations highlight the effectiveness of key molecules like (*E*)-citral, citronellyl tiglate, linalool, and α-pinene, which exhibit strong adsorption energies and favorable electronic properties for forming a protective barrier. GEO shows great promise as an eco-friendly corrosion inhibitor, presenting an effective alternative to synthetic inhibitors, especially in acidic environments.

Table 12. The optimal configurations of simulations for the various molecules in gas and aqueous phases obtained by Monte Carlo.

Geraniol	**Geranyl formate**	**Germacrene D**	**Geranyl propionate**	***iso*-Menthone**	**α-Pinene**
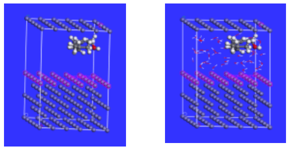	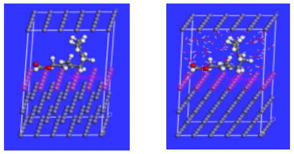	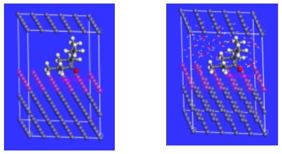	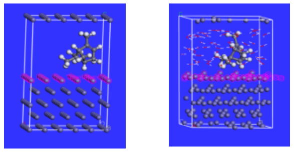	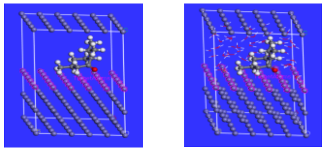	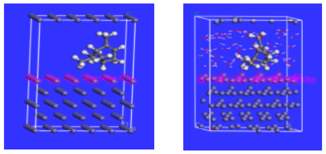
β-Citronellol	***trans*-Rose oxide**	**α-Terpineol**	**Neryl formate**	**Geranyl butyrate**	**Citronellyl acetate**
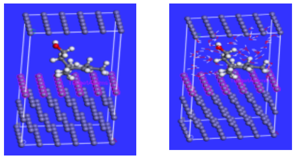	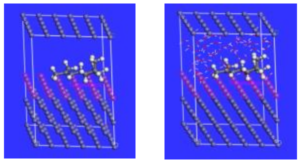	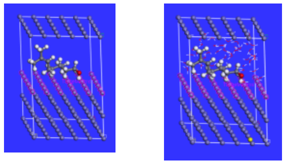	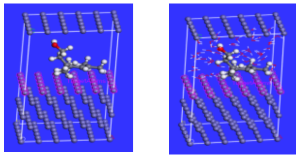	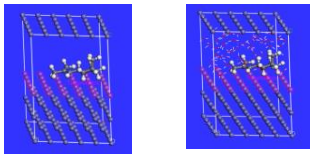	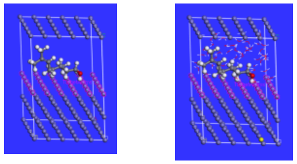
Citronellyl formate	**Nerol**	**α-Muurolene**	**α-Selinene**	**Citronellol**	**β-Bourbonene**
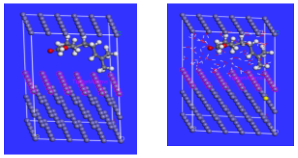	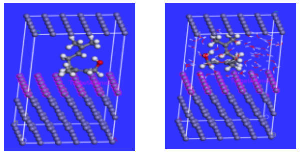	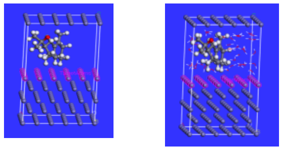	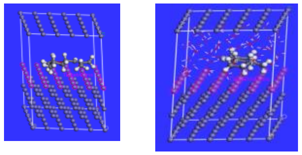	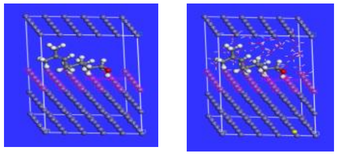	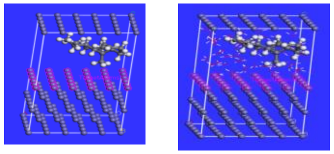
Linalool	**γ-Cadinene**	**Viridiflore**	**Citronellyl tiglate**	**(*E*)-Citral**	**Geranyl tiglate**
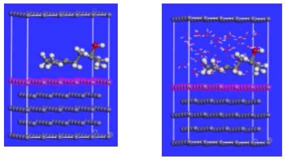	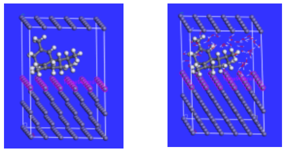	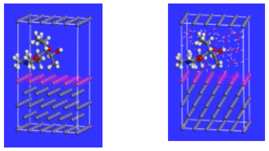	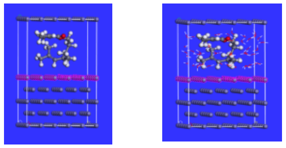	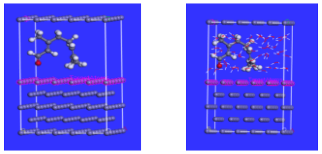	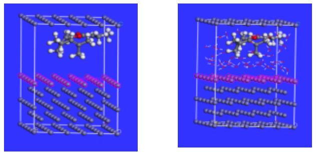
10-*epi*-*g*-Eudesmol	***cis*-Rose oxide**	***trans*-Caryophyllene**	**Citronellyl ester**	**α-Costol**	**2-Phenethyl tiglate**
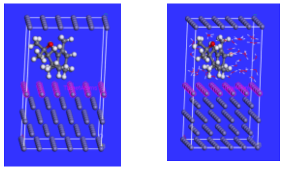	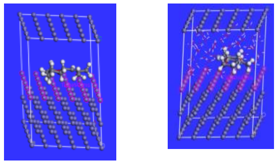	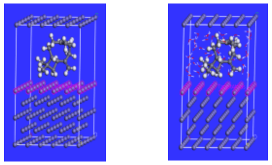	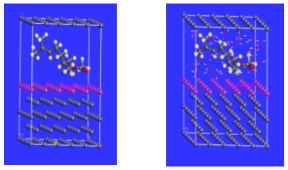	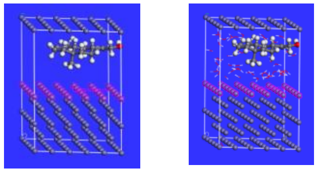	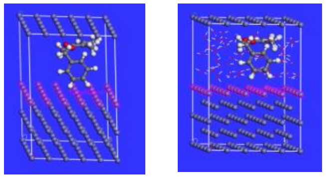

References

1. L. Afia, O. Benali, R. Salghi, E.E. Ebenso, S. Jodeh, M. Zougagh and B. Hammouti, Steel Corrosion Inhibition by Acid Garlic Essential Oil as a Green Corrosion Inhibitor and Sorption Behavior, *Int. J. Electrochem. Sci*., 2014, **9**, 8392–8406. doi: 10.1016/S1452-3981(23)11055-8
2. M. Oubahou, M. Rbaa, H. Lgaz, D. Takky, Y. Naimi, A.A. Alrashdi and H.-S. Le, Exploring sustainable corrosion inhibition of copper in saline environment: An examination of hydroquinazolinones via experimental and ab initio DFT simulations, *Arabian J. Chem*., 2024, **17**, 105716. doi: 10.1016/j.arabjc.2024.105716
3. S.El Harrari, S. Ayoub, D. Takky and Y. Naimi, Electrochemical Investigation of Terbinafine ($C_{21}H_{25}N$) as a Corrosion Inhibitor for Copper in a Molar Sulfuric Acid Solution, *Egypt. J. Chem*`., 2023, **66**, no. 6, 487–492.
4. M. Belhadi, M. Oubahou, I. Hammoudan, A. Chraka, M. Chafi and S. Tighadouini, A comprehensive assessment of carbon steel corrosion inhibition by 1,10-phenanthroline in the acidic environment: insights from experimental and computational studies, *Environ. Sci. Pollut. Res*., 2024, **31**, 62038–62055. doi: 10.1007/s11356-023-27582-1
5. W. Zriouel, A. Bentis, S. Majid, B. Hammouti and S. Gmouh, Blue Tansy essential oil as eco-friendly corrosion inhibitor of mild steel in 1 M HCl solution: Electrochemical study, DFTB computation and Monte Carlo simulation, *Int. J. Corros. Scale Inhib*., 2023, **12**, no. 3, 1136–1161. doi: 10.17675/2305-6894-2023-12-3-19
6. W. Daoudi, A. El Aatiaoui, N. Falil, M. Azzouzi, A. Berisha, L.O. Olasunkanmi, O. Dagdag, E.E. Ebenso, M. Koudad, A. Aouinti, M. Loutou and A. Oussaid, Essential oil of Dysphania ambrosioides as a green corrosion inhibitor for mild steel in HCl solution, *J. Mol. Liq*., 2022, **363**, 119839. doi: 10.1016/j.molliq.2022.119839
7. G. Cristofari, M. Znini, L. Majidi, J. Costa, B. Hammouti and J. Paolini, Helichrysum italicum subsp. Italicum Essential Oil as Environmentally Friendly Inhibitor on the Corrosion of Mil Steel in Hydrochloric Acid, *Int. J. Electrochem. Sci*., 2012, **7**, 9024–9041. doi: 10.1016/S1452-3981(23)18048-5
8. R.T. Loto and M.M. Solomon, Application of ginger and grapefruit essential oil extracts on the corrosion inhibition of mild steel in dilute 0.5 M H_2SO_4 electrolyte, *Sci. Afr*., 2023, **19**, 01489. doi: 10.1016/j.sciaf.2022.e01489
9. W. Zriouel, A. Bentis, S. Majid, B. Hammouti, S. Gmouh, P.S. Umoren and S.A. Umoren, The Blue Tansy Essential Oil–Petra/Osiris/ Molinspiration (POM) Analyses and Prediction of Its Corrosion Inhibition Performance Based on Chemical Composition, *Sustainability*, 2023, **15**, 14274. doi: 10.3390/su151914274
10. *Materials Studio version 2020*, BIOVIA, San Diego, CA, USA, 2020.
11. W. Zriouel, A. Bentis, S. Majid, B. Hammouti and S. Gmouh, Computational study and predictive investigation of the inhibitory behavior of Geranium essential oil: DFT calculation, Monte Carlo simulation and POM analyses, *Eur. Chem. Bull*., 2023, **12**, no. 12, 2978–3002.

12. M. Oubahou, A. El Aloua, N. Benzbiria, S. El Harrari, D. Takky, Y. Naimi, A. Zeroual, Sh. Wang, A. Syed and M.E. Belghiti, Electrochemical, thermodynamic and computational investigation of the use of an expired drug as a sustainable corrosion inhibitor for copper in 0.5 M H_2SO_4, *Mater. Chem. Phys.*, 2024, **323**, 129642. doi: 10.1016/j.matchemphys.2024.129642
13. G. Xia, X. Jiang, L. Zhou, Y. Liao, H. Wang, Q. Pu and J. Zhou, Synergic effect of methyl acrylate and N-cetylpyridinium bromide in N-cetyl-3-(2- methoxycarbonylvinyl) pyridinium bromide molecule for X70 steel protection, *Corros. Sci.*, 2015, **94**, 224–236. doi: 10.1016/j.corsci.2015.02.005
14. K. Berdimuradov, E. Berdimurodov, B. El Ibrahimi, M. Demir, S.G. Colak, B. Tüzün, M. Rakhmatullaeva, M. Diyorova, D. Axtamov and Q. Husenov, Enhanced Corrosion-Inhibition performance of amino Gossypol: A comprehensive theoretical study, *Comput. Theor. Chem.*, 2024, **1241**, 114920. doi: 10.1016/j.comptc.2024.114920
15. I.B. Obot, S. Kaya, C. Kaya and B. Tüzün, Density Functional Theory (DFT) modeling and Monte Carlo simulation assessment of inhibition performance of some carbohydrazide Schiff bases for steel corrosion, *Physica E*, 2016, **80**, 82–90. doi: 10.1016/j.physe.2016.01.024
16. A.N. Venancio, L. Menini, D.N. Maronde, E.V. Gusevskaya and L.A. Parreira, Palladium catalyzed oxidation of biorenewable β-citronellol and geraniol for the synthesis of polyfunctionalized fragrances, *Mol. Catal.*, 2021, **504**, 111449. doi: 10.1016/j.mcat.2021.111449
17. M. Oubahou, M. Rbaa, D. Takky, Y. Naimi, A.A. Alrashdi and H. Lgaz, Elucidating the role of novel halogenated hydroquinazolinone derivatives in mitigating copper corrosion in saline conditions: A joint assessment of experimental outcomes and computational analysis, *J. Mol. Liq.*, 2023, **390**, 122966. doi: 10.1016/j.molliq.2023.122966
18. M.A. Quraishi, D.S. Chauhan and V.S. Saji, 2 – Experimental methods of inhibitor evaluation, *Heterocyclic Organic Corrosion Inhibitors*, 2020, **2020**, 21–57. doi: 10.1016/b978-0-12-818558-2.00002-3
19. P. Vashishth, H. Bairagi, R. Narang, S.K. Shukla, L.O. Olasunkanmi, E.E. Ebenso and B. Mangla, Experimental investigation of sustainable Corrosion Inhibitor Albumin on low-carbon steel in 1N HCl and 1N H_2SO_4, *Results in Surfaces and Interfaces*, 2023, **13**, 100155. doi: 10.1016/j.rsurfi.2023.100155
20. S.A. Umoren, M.J. Banera, T. Alonso-Garcia, C.A. Gervasi and M.V. Mirífico, Inhibition of mild steel corrosion in HCl solution using chitosan, *Cellulose*, 2013, **20**, no. 5, 2529–2545. doi: 10.1007/S10570-013-0021-5

21. M. Rbaa, A. Abousalem, Z. Rouifi, R. Benkaddour, P. Dohare, M. Lakhrissi, I. Warad, B. Lakhrissi and A. Zarrouk, Synthesis, antibacterial study and corrosion inhibition potential of newly synthesis oxathiolan and triazole derivatives of 8-hydroxyquinoline: Experimental and theoretical approach, *Surf. Interfaces*, 2020, **19**, 100468. doi: 10.1016/j.surfin.2020.100468
22. E. Ech-Chihbi, M. Beniken, R. Salim, M. Sfaira, B. Hammouti, M. Ebn Touhami, M.A. Mohsin and M. Taleb, Adsorption behavior and corrosion inhibition mechanism of a polyacrylamide on C–steel in 0.5 M H_2SO_4: Electrochemical assessments and molecular dynamic simulation, *J. Mol. Liq.*, 2022, **348**, 118022. doi: 10.1016/j.molliq.2021.118022
23. A. Singh, K.R. Ansari, M.A. Quraishi, S. Kaya and S. Erkan, Chemically modified guar gum and ethyl acrylate composite as a new corrosion inhibitor for reduction in hydrogen evolution and tubular steel corrosion protection in acidic environment, *Int. J. Hydrogen Energy*, 2021, **46**, no. 14, 9452–9465. doi: 10.1016/j.ijhydene.2020.12.103
24. C. Verma, D.K. Verma, E.E. Ebenso and M.A. Quraishi, Sulfur and phosphorus heteroatom-containing compounds as corrosion inhibitors: An overview, *Heteroat. Chem.*, 2018, **29**, no. 4, e21437. doi: 10.1002/hc.21437
25. P. Refait, C. Rahal and M. Masmoudi, Corrosion inhibition of copper in 0.5 M NaCl solutions by aqueous and hydrolysis acid extracts of olive leaf, *J. Electroanal. Chem.*, 2020, **859**, 113834. doi: 10.1016/j.jelechem.2020.113834
26. M.S. Morad and A.M.K. El-Dean, 2,2′-Dithiobis(3-cyano-4,6-dimethylpyridine): A new class of acid corrosion inhibitors for mild steel, *Corros. Sci.*, 2006, **48**, no. 11, 3398–3412. doi: 10.1016/j.corsci.2005.12.006
27. D.I. Njoku, P.C. Okafor, H. Lgaz, K.J. Uwakwe, E.E. Oguzie and Y. Li, Outstanding anticorrosion and adsorption properties of 2-amino-6-methoxybenzothiazole on Q235 and X70 carbon steels : Effect of time, XPS, electrochemical and theoretical considerations, *J. Mol. Liq.*, 2021, **324**, 114663. doi: 10.1016/j.molliq.2020.114663
28. M. El Faydy, R. Touir, M. Ebn Touhami, A. Zarrouk, C. Jama, B. Lakhrissi, L.O. Olasunkanmi, E.E. Ebenso and F. Bentiss, Corrosion inhibition performance of newly synthesized 5-alkoxymethyl-8-hydroxyquinoline derivatives for carbon steel in 1 M HCl solution: experimental, DFT and Monte Carlo simulation studies, *Phys. Chem. Chem. Phys.*, 2018, **20**, no. 30, 20167–20187. doi: 10.1039/C8CP03226B
29. R.L. Minagalavar, S.K. Rajappa, M.R. Rathod and A.M. Sajjan, Investigation of corrosion inhibition performance of expired fluconazole drug on mild steel in 0.5 M H_2SO_4 medium, *J. Mol. Liq.*, 2023, **391**, 123291. doi: 10.1016/j.molliq.2023.123291
30. S.A. Umoren, A.A. AlAhmary, Z.M. Gasem and M.M. Solomon, Evaluation of chitosan and carboxymethyl cellulose as eco-friendly corrosion inhibitors for steel, *Int. J. Biol. Macromol.*, 2018, **117**, 1017–1028. doi: 10.1016/j.ijbiomac.2018.06.014

---

31. N. Errahmany, M. Rbaa, A.S. Abousalem, A. Tazouti, M. Galai, El.H.El Kafssaoui, M. Ebn Touhami, B. Lakhrissi and R. Touir, Experimental, DFT calculations and MC simulations concept of novel quinazolinone derivatives as corrosion inhibitor for mild steel in 1.0 M HCl medium, *J. Mol. Liq.*, 2020, **312**, 113413. doi: 10.1016/j.molliq.2020.113413
32. I. Dehri and M. Özcan, The effect of temperature on the corrosion of mild steel in acidic media in the presence of some sulphur-containing organic compounds, *Mater. Chem. Phys.*, 2006, **98**, no. 2–3, 316–323. doi: 10.1016/j.matchemphys.2005.09.020
33. B. Tan, A. Fu, L. Guo, Y. Ran, J. Xiong, R. Marzouki and W. Li, Insight into anti-corrosion mechanism of Dalbergia odorifera leaves extract as a biodegradable inhibitor for X70 steel in sulfuric acid medium, *Ind. Crops Prod.*, 2023, **194**, 116106. doi: 10.1016/j.indcrop.2022.116106
34. E.S.M. Sherif, Effects of 2-amino-5-(ethylthio)-1,3,4-thiadiazole on copper corrosion as a corrosion inhibitor in 3% NaCl solutions, *Appl. Surf. Sci.*, 2006, **252**, no. 24, 8615–8623. doi: 10.1016/j.apsusc.2005.11.082
35. A. Belkheiri, K. Dahmani, Z. Aribou, O. Kharbouch, E. Nordine, E.A. Allah, M. Galai, M. Ebn Touhami, M.K. Al-Sadoon, B.M. Al-Maswari and Y. Ramli, In-depth study of a newly synthesized imidazole derivative as an eco-friendly corrosion inhibitor for mild steel in 1 M HCl: Theoretical, electrochemical, and surface analysis perspectives, *Int. J. Electrochem. Sci.*, 2024, **19**, no. 10, 100768. doi: 10.1016/j.ijoes.2024.100768
36. P. Vashishth, H. Bairagi, R. Narang, S.K. Shukla, L.O. Olasunkanmi, E.E. Ebenso and B. Mangla, Experimental investigation of sustainable Corrosion Inhibitor Albumin on low-carbon steel in 1N HCl and 1N H_2SO_4, *Results in Surfaces and Interfaces*, 2023, **13**, 100155. doi: 10.1016/j.rsurfi.2023.100155
37. S.A. Umoren, M.J. Banera, T. Alonso-Garcia, C.A. Gervasi and M.V. Mirífico, Inhibition of mild steel corrosion in HCl solution using chitosan, *Cellulose*, 2013, **20**, no. 5, 2529–2545. doi: 10.1007/S10570-013-0021-5
38. A. Chaouiki, M. Chafiq, Y.G. Ko, A.H. Al-Moubaraki, F. Thari, R. Salghi, K. Karrouchi, K. Bougrin, I.H. Ali and H. Lgaz, Adsorption Mechanism of Eco-Friendly Corrosion Inhibitors for Exceptional Corrosion Protection of Carbon Steel: Electrochemical and First-Principles DFT Evaluations, *Metals*, 2022, **12**, no. 10, 1598. doi: 10.3390/met12101598
39. I.M. Chung, K. Kalaiselvi, A. Sasireka, S.H. Kim and M. Prabakaran, Anticorrosive property of Spiraea Cantoniensisis extract as an eco-friendly inhibitor on mild steel surface in acid medium, *J. Dispers. Sci. Technol.*, 2019, **40**, no. 9, 1326–1337. doi: 10.1080/01932691.2018.1511435
40. I.A. Zaafarany, Corrosion inhibition of 1018 carbon steel in hydrochloric acid using Schiff base compounds, *Int. J. Corros. Scale Inhib.*, 2014, **3**, no. 1, 12–27. doi: 10.17675/2305-6894-2014-3-1-012-027

41. A. Hamdy and N.S. El-Gendy, Thermodynamic, adsorption and electrochemical studies for corrosion inhibition of carbon steel by henna extract in acid medium, *Egypt. J. Pet.*, 2013, **22**, no. 1, 17–25. doi: 10.1016/j.ejpe.2012.06.002
42. Y. Toubi, Y. Hakmaoui, R. EL Ajlaoui, F. Abrigach, D. Zahri, S. Radi, El M. Rakib, H. Lgaz and B. Hammouti, Unexpected efficient one-pot synthesis, DFT calculations, and docking study of new 4-hydroxy-2H-chromen-2-one derivatives predicted to target SARS-CoV-2 spike protein, *J. Mol. Struct.*, 2024, **1295**, 136789.
43. C.T. Ser, P. Žuvela and M.W. Wong, Prediction of corrosion inhibition efficiency of pyridines and quinolines on an iron surface using machine learning-powered quantitative structureproperty relationships, *Appl. Surf. Sci.*, 2020, **512**, 145612. doi: 10.1016/j.apsusc.2020.145612
44. S. Kaya, L. Guo, C. Kaya, B. Tüzün, I.B. Obot, R. Touir and N. Islam, Quantum chemical and molecular dynamic simulation studies for the prediction of inhibition efficiencies of some piperidine derivatives on the corrosion of iron, *J. Taiwan Inst. Chem. Eng.*, 2016, **65**, 522–529. doi: 10.1016/j.jtice.2016.05.034
45. C. Verma, H. Lgaz, D.K. Verma, E.E. Ebenso, I. Bahadur and M.A. Quraishi, Molecular dynamics and Monte Carlo simulations as powerful tools for study of interfacial adsorption behavior of corrosion inhibitors in aqueous phase: A review, *J. Mol. Liq.*, 2018, **260**, 99–120. doi: 10.1016/j.molliq.2018.03.045

♦ ♦ ♦